NASA TECHNICAL NOTE

$C. 1$

NASA TN D-5134

OVERALL PERFORMANCE OF A TANDEM-BLADED INDUCER TESTED IN WATER

by Richard F. Soltis, Donald C. Urasek, and Max J. Miller

Lewis Research Center
Cleveland, Ohio

OVERALL PERFORMANCE OF A TANDEM-BLADED INDUCER
TESTED IN WATER

by Richard F. Soltis, Donald C. Urasek, and Max J. Miller
May 1969

Page 2:   The second sentence in paragraph 4 is incomplete. It should read "The inducer, which was designed for NASA by Dr. Julius Kolin under NASA contract NAS 3-3728, was 6.5 inches (16.5 cm) in diameter and consisted of three tandem blades in both portions of the inducer."

NASA TN D-5134

OVERALL PERFORMANCE OF A TANDEM-BLADED

INDUCER TESTED IN WATER

By Richard F. Soltis, Donald C. Urasek, and Max J. Miller

Lewis Research Center
Cleveland, Ohio

NATIONAL AERONAUTICS AND SPACE ADMINISTRATION

ABSTRACT

A 6.5-inch (16.5-cm) diameter inducer composed of tandem blades was tested. Design values of head rise coefficient and flow coefficient were 0.303 and 0.109, respectively. At design flow the noncavitating measured head rise coefficient was 0.278 at a hydraulic efficiency of 0.88. Cavitation caused the head rise to drop off at a suction specific speed of approximately 20 000. It is speculated that cavitation performance could be improved by reducing the blade thickness in the leading edge regions of both blades. The occurrence of cavitation is illustrated in still photographs and the visual observations are correlated with measured results. Small changes to slot geometry were made and resulted in relatively small changes in performance.

OVERALL PERFORMANCE OF A TANDEM-BLADED
INDUCER TESTED IN WATER

by Richard F. Soltis, Donald C. Urasek, and Max J. Miller

Lewis Research Center

SUMMARY

A 6.5-inch (16.5-cm) diameter inducer composed of tandem blades was tested in cold water. The inducer was designed to produce a head rise coefficient of 0.303 at an ideal inlet flow coefficient of 0.109.

At design flow the inducer achieved a head rise coefficient of 0.278 at a hydraulic efficiency of 0.88. Cavitation caused a 10-percent decrease in head rise from the non-cavitating level at a suction specific speed of approximately 20 000. This modest suction performance is attributed to excessive blade thickness in the inlet portions of both the front and rear blades.

A relatively high efficiency (>80 percent) was maintained over a large portion of the flow range. At a flow of approximately 84 percent of design, measurements indicated a reverse, or eddy, flow region in the flow entering the blade tip. As flow was further reduced, the radial extent of the eddy region increased.

Visual observations of cavitation generally indicated that the inducer head rise was not affected until the cavitation extended into the passages of the rear blades.

Small changes to the slot geometry were made and midspan head rise measurements from three configurations compared. As the overlap of the two blades was increased, the noncavitating head rise increased. The slot geometry changes did not measurably affect the cavitation performance.

INTRODUCTION

Most pumps requiring high suction specific speed operation have an inducer stage or inducer section. The function of the inducer is to produce a head rise sufficient to allow the main pump to operate relatively cavitation-free, despite the occurrence of cavitation within the inducer. Some reduction in overall pump size and weight may be realized if

the inducer head rise can be increased without sacrificing suction performance. However, these two characteristics are not compatible in that the high blade loading required for high head rise capability is also conducive to greater amounts of cavitation with associated lower suction performance. One compromise in design is to consider the inducer in two portions. The inlet portion is lightly loaded to realize good suction performance with a modest head rise. The latter portion is highly loaded in order to maximize the overall head rise of the inducer. This approach has been applied to variable-lead helical bladed inducers. In the lightly loaded inlet portions of the individual blade, changes of lead are small, while in the highly loaded latter portion of the blade, the changes of lead are large.

Another approach is to make each portion of the inducer a separate rotating blade row. Reference 1 reports an example inducer composed of two separate tandem-mounted blade rows. The first rotating row consisted of three long chord, lightly loaded blades, whereas the second tandem-mounted blade row consisted of 19 short-chord, higher loaded blades. This tandem design achieved a head rise coefficient of 0.32 at a hydraulic efficiency of over 80 percent. A suction specific speed of approximately 27 000 was attained before a significant dropoff in head rise due to cavitation was observed.

Separating the two portions of the inducer into separate blade rows offers the advantage of starting new blade surface boundary layers as the fluid enters the highly loaded portion of the inducer. This is desirable for flow through an inducer since the collapse of the blade surface cavity in the inlet portion of the inducer could leave the blade surface boundary layer in poor condition to traverse the highly loaded portion of the blade row without separation.

Good performance results have been reported from investigations of slotted and tandem blades as applied to both rotating and stationary blade rows (see refs. 2 to 4). These results suggest incorporating the two portions of the inducer into a tandem blade configuration which has the advantages of the new boundary layer on the rear blade as previously noted plus the opportunity to further aid the suction surface boundary layer flow on the rear blade by controlling the flow through the slot formed by the two blades.

The experimental investigation reported herein demonstrates the application of tandem blades to a pump inducer. The inducer, which was designed for NASA under contract NAS3-3728, was 6.5 inches (16.5 cm) in diameter and consisted of three tandem blades in both portions of the inducer. The design head rise coefficient of 0.303 is more than twice that obtained from more conventional flat plate helical inducers (head rise coefficient ~0.12) (refs. 5 to 7).

The inducer steady-state overall performance under both cavitating and noncavitating flow conditions is presented. Visual observations are correlated with measured data. The effects of small changes in slot geometry on performance as well as limited measurements defining the outer wall boundary layer at the blade inlet and outlet are also presented.

2

APPARATUS AND PROCEDURE

Test Pump

The following inducer design specifications were dictated by the existing test facility (all symbols are defined in appendix A).

Inlet tip diameter d_t, in. (cm) 6.5 (16.5)
Inlet hub-tip radius ratio r_h/r_t 0.4
Ratio of inducer outlet area to inlet area A_2/A_1 . . . . 0.5
Maximum axial depth, in. (cm) 4.5 (11.4)

The outer casing at the test section incorporated a linear taper from a diameter of 6.5 inches (16.5 cm) near the inducer inlet to a value of 6.175 inches (15.7 cm) near the outlet. The inducer tip diameter was matched to this taper.

Hydrodynamic design values, as supplied by the designer, included

Ideal inlet flow coefficient, φ_{id} 0.109
Head rise coefficient, $\overline{\psi}$ 0.303

As discussed in reference 4, the inlet flow coefficient, when combined with r_h/r_t of 0.4 and an inlet flow angle (β_1) of 0°, is the optimum value for a suction specific speed of approximately 30 000.

The inducer had three blades. Each blade was composed of a relatively long-chord front blade (7.74 in. or 19.66 cm at tip) and a short-chord rear blade (2.75 in. or 6.98 cm at tip). The front and rear blades were fabricated individually from separate material blanks. This permitted some freedom to vary the slot geometry between the two blades during testing. It also minimized redesign if different setting angles of the rear blades were desired. The hub radius increased across the inducer as needed to meet the required area changes and comply with the specified tip taper. A photograph of the inducer is shown in figure 1.

The blade section geometry for the element on the tip diameter cylindrical surface (d_c = 6.5 in. or 16.5 cm) for both blades is specified. The remainder of the blade sections are defined by radial lines from this tip section. The geometry of the blade tip section for both front and rear blades is given in figure 2. The blade suction and pressure surfaces are helical surfaces with different leads which are faired in the inlet portions according to the given coordinate schedule. The two helical surfaces are separated by a specified thickness value. The chord-wise distance of fairing of the pressure surfaces of both front and rear blades is very small so that this surface remains essentially
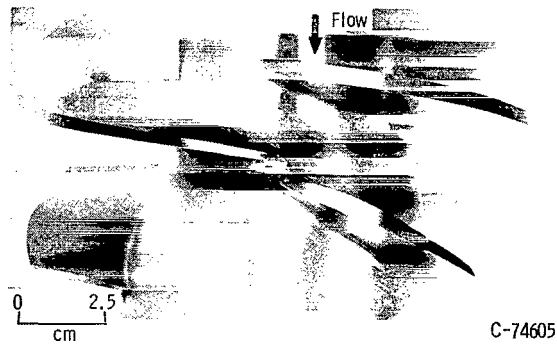
Figure 1. - Tandem inducer.

| Rear plane						Front plane					
Directional coordinate											
x		y		-y		x		y		-y	
in.	cm	in.	cm	in.	cm	in.	cm	in.	cm	in.	cm
0	0	0.042	0.107	0.042	0.107	0	0	0.039	0.099	0.039	0.099
.055	.140	.074	.188	.023	.058	.010	.025	.046	.117	.026	.066
.108	.274	.094	.239	.018	.046	.150	.381	.087	.221	.015	.038
.240	.610	.135	.343	.009	.023	.215	.546	.103	.262	.009	.023
.381	.968	.166	.422	.002	.005	.320	.813	.122	.310	.004	.010
.520	1.321	.183	.465	0	0	.500	1.270	.143	.363	0	0
.790	2.007	.204	.518			.950	2.413	.169	.429		
1.050	2.667	.203	.516			1.300	3.302	.180	.457		
1.431	3.635	.180	.457			2.030	5.156	.191	.485		
						2.790	7.087	.194	.493		
						3.550	9.017	.178	.452		
						7.640	19.406	.081	.206		
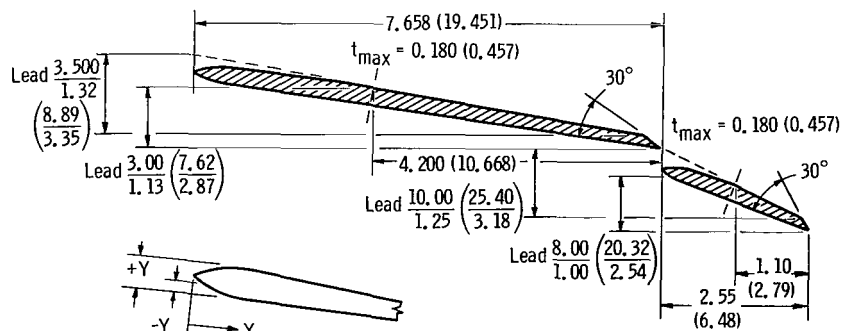
Figure 2. - Blade section (front and rear blades) at 6.5-inch (16.51-cm) tip diameter. Leading edge radius, 0.010 inch (0.025 cm).

a flat plate. The fairing of the suction surface extends over approximately the forward half of the blade section. Thus, in this forward portion of blade section a locus of mid-points between pressure and suction surfaces would describe a line with some camber. The blade was fabricated with essentially a constant thickness from hub to tip.

Test Facility

The tandem inducer was tested in the Lewis waterpump test facility. A sketch of this closed-loop test facility is shown in figure 3. Prior to testing, the water is circulated through the degasifying and filtering system. The gas content is reduced and maintained to less than 3 parts per million by weight and the filter is capable of removing particles over 5 micrometers in size. The test facility is discussed in more detail in reference 8.
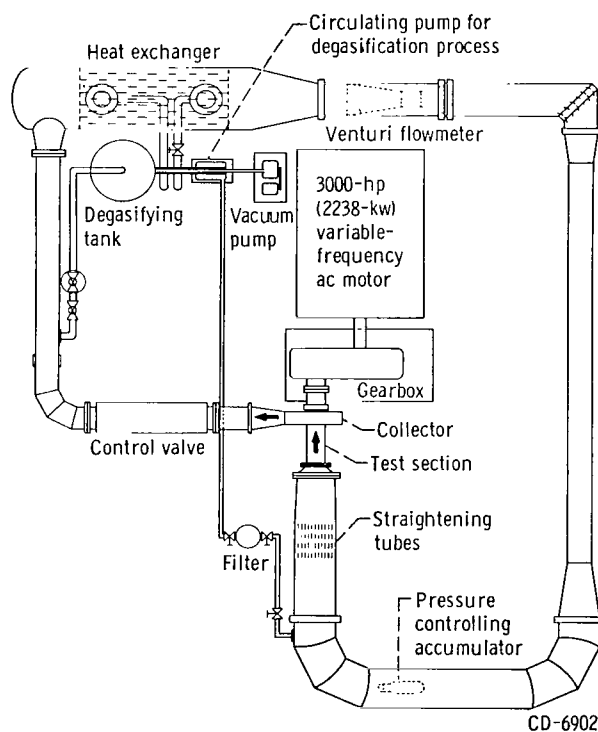
Figure 3. - Lewis water tunnel.

Test Procedure and Instrumentation

Flow conditions were measured at the inducer inlet and outlet (approx 0.5 in. 1.27 cm) upstream and downstream of the blade leading and trailing edges, respectively) while the inducer was operated: (1) over a range of flow rates at constant values of rotative speed and net positive suction head H_{sv}; and (2) over a range of net positive suction heads at constant values of rotative speed and flow. Survey probes measured total pressure, static pressure, and flow angle across the flow annulus at radial positions located approximately 10, 30, 50, 70, and 90 percent of the annulus height from the outer wall. The equations used to calculate selected flow and performance parameters are presented in appendix B.

Photographs of the survey probes are shown in figure 4. Total pressure and flow angle were measured with the cobra probe (fig. 4(a)), and static pressure with the wedge probe (fig. 4(b)). Each probe had associated null-balancing, stream-direction-

C-65-1423   C-67-3754   C-67-3755   C-67-3118   C-67-3117

Front view   Side view   Front view   Side view

(a) Cobra probe.   (b) Static-pressure wedge.   (c) Boundary-layer probe measuring angle and total pressure.
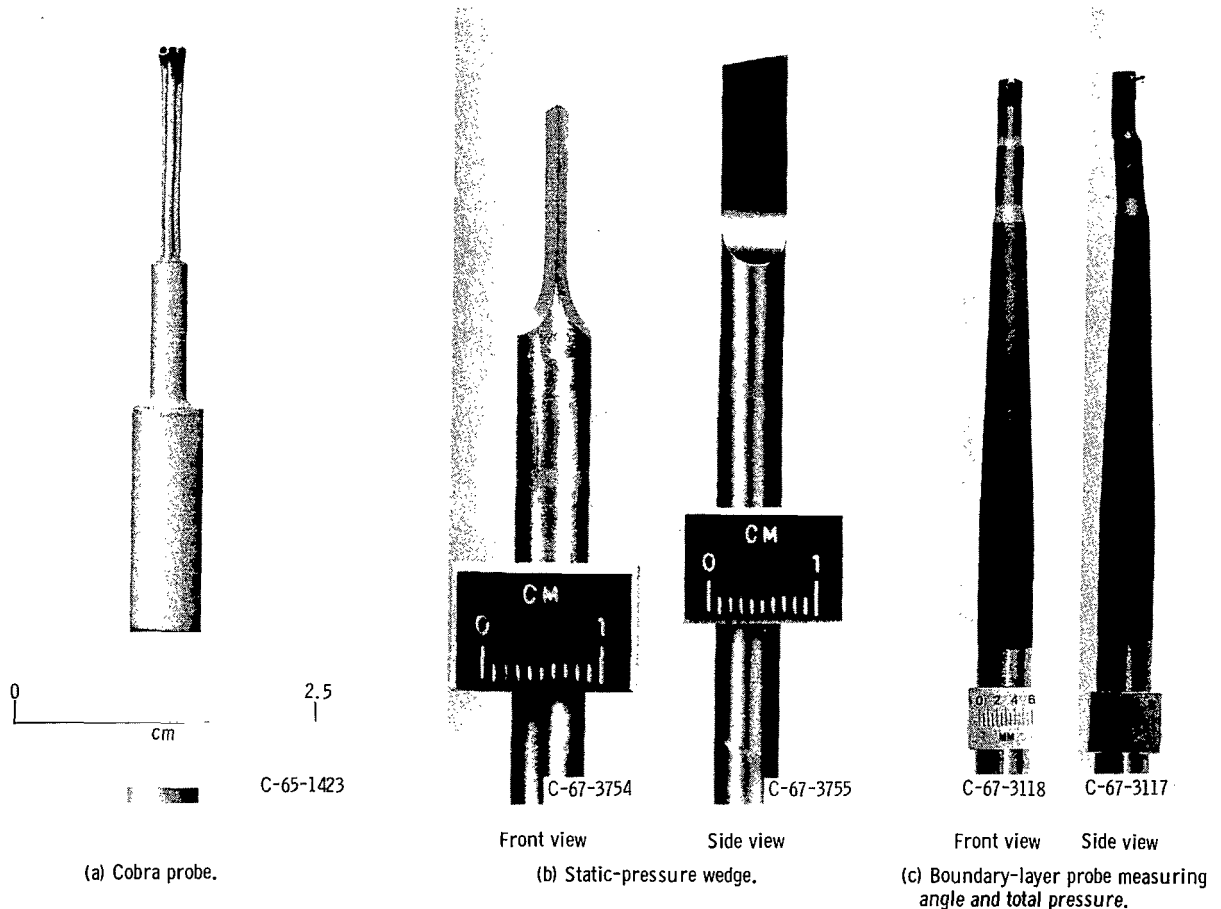
Figure 4. - Probes.

sensitive equipment that automatically alined the probe to the direction of flow. Each wedge static probe was calibrated in a low speed air tunnel. Additional measurements included a Venturi flowmeter to measure flow rate and an electronic speed counter used in conjunction with a magnetic pickup to measure rotor rpm.

Distributions of total pressure and flow angle across the boundary layer on the outer walls were measured with the probe shown in figure 4(c). Boundary layer surveys were taken at four flow coefficient values from 0.10 to 0.15 under noncavitating flow conditions.

Data Accuracy and Reliability

Minimum errors in the data based on the inherent accuracies of the measurement and recording systems are estimated to be as follows:

Flow rate Q_v, percent of design flow . . . . ± 1.0
Rotative speed N, percent . . . . ± 0.5
Head rise ΔH, percent at design flow . . . . ± 1.0
Velocity head $V^2/2g$, percent at design flow . . . . ± 1.5
Flow angle β_1, deg . . . . ± 1.0
Net positive suction head H_{sv}, ft . . . . ± 1.0

Unsteady flows, circumferential variations in flow, and other time or space gradients affecting the measurements were not evaluated.

A partial check on any circumferential variations of flow conditions with changes in flow rate was made by inserting probes that measured total pressure and flow angle at three circumferential locations (see fig. 5) at the outlet measuring station.

The three probes were positioned at the midspan location. Measured values of outlet total head and flow angle are shown in figures 5 and 6, respectively. Over the entire flow range, all total pressures were within 1.0 percent of an average value represented by the faired curve. The flow angles on two of the probes were within $1\frac{1}{2}^{\circ}$ of each other over the complete flow range. The measured flow angle from the third probe was consistently lower than the other two by approximately $1\frac{1}{2}^{\circ}$. From these results it was concluded that the flow from the inducer could be considered essentially axisymmetric.

A measure of the accuracy of the data is also provided by comparing the flow rates as determined from integrated survey measurements at inlet and outlet of the inducer to
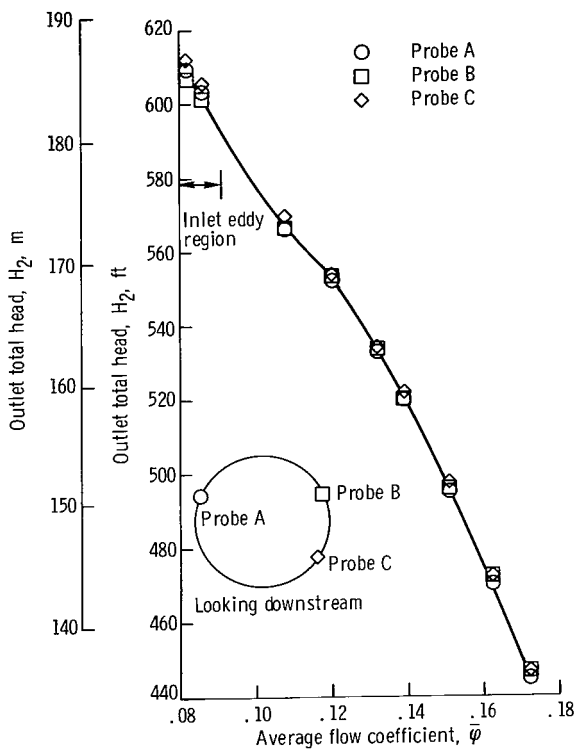
Figure 5. - Midpassage outlet total pressure at three circumferential locations. Rotative speed, 5415 rpm; net positive suction head, 384 feet (117 m).
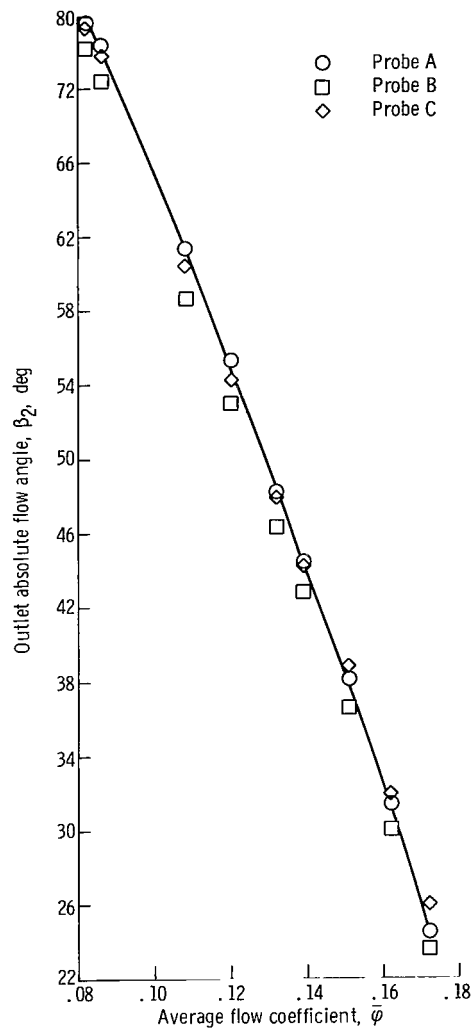

Figure 6. - Midpassage outlet flow angle at three circumferential locations. Rotative speed, 5415 rpm; net positive suction head, 384 feet (117 m).
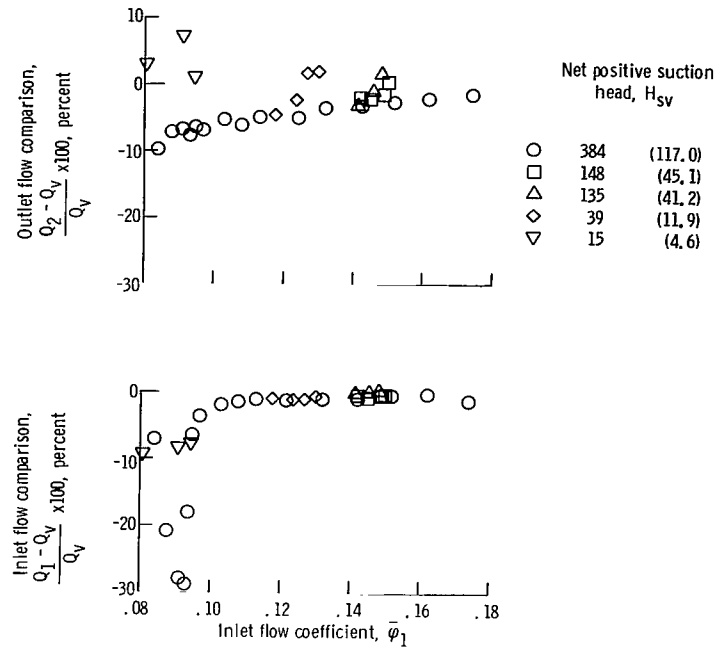
8

Figure 7. - Comparison of integrated flows at inducer inlet and outlet with those measured by Venturi meter.

the flow rate measured with the Venturi meter. The flow comparisons are presented in figure 7 in the form

$$\frac{Q_{1,2} - Q_v}{Q_v} \times 100$$

and plotted as a function of average inlet flow coefficient $\overline{\varphi}_1$. At flow coefficients greater than 0.10, the integrated flows at the inducer inlet are within 2 percent of the Venturi flows for all levels of H_{sv}. At flow coefficients less than 0.10, the integrated flows deviate significantly from the Venturi flows. This is attributed to a reverse flow region which forms in the inlet tip region at $\overline{\varphi} < 0.10$ that makes it difficult to obtain a meaningful integration of flow. Also, at the low inlet pressures, cavitation forms on the wedge static probe.

At the inducer outlet, the integrated flows compare with the Venturi flows within a few percent at the high flows where the velocities are the largest. As the flow is reduced, the percent deviation of the two flow measurements increases consistently to values of approximately 0.07. Some of this percentage increase between the two flow calculations is expected due to lower through-flow velocities and increases in pressure gradients, in boundary layer thickness, in secondary flows, etc.; however, the flow checks generally indicate a reasonable agreement of measured data.

9

RESULTS AND DISCUSSION

The presentation is generally divided into results obtained under noncavitating and cavitating conditions. Herein, cavitating results mean that a measurable reduction in head rise from the noncavitating value has been observed. All data presented is from the design tandem blade configuration (tandem I) unless specifically noted.

Noncavitating Average Performance

The average noncavitating inducer performance is presented in figure 8. Head rise coefficient $\bar{\psi}$ and efficiency $\bar{\eta}$ are plotted as a function of flow coefficient $\bar{\varphi}$. Head
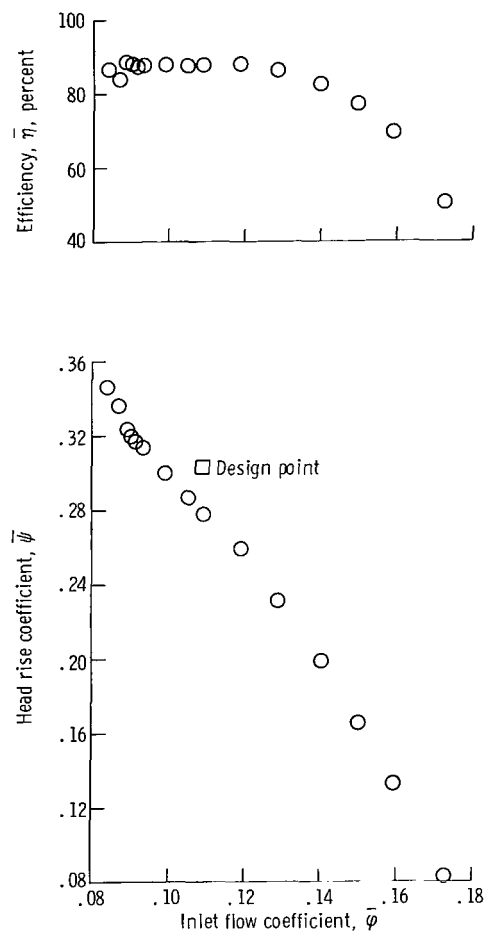
Figure 8. - Inducer overall performance at noncavitating conditions. Net positive suction head, 384 feet (117 m).

rise coefficient and efficiency are mass-averaged values. Flow coefficient is an average value based on measured flow and inlet geometric area as defined by equation (B5) of appendix B.

From the casing boundary layer measurements (see appendix C), a flow blockage factor of 2.20 percent was determined for design flow at the inducer inlet. (A flow blockage factor of 2.29 percent was computed at the blade outlet.) Thus, the design inlet flow diagrams should be achieved at a measured average flow coefficient of

$$\overline{\varphi} = 0.978 \ \overline{\varphi}_{id} = 0.107$$

This flow coefficient of 0.107 is used hereinafter as the design value in comparison of measured and design parameters. At $\overline{\varphi} = 0.107$, the measured head rise coefficient of 0.278 is slightly below the design value of 0.303. Hydraulic efficiency at this operating point was approximately 88 percent.

Over the flow range covered $\overline{\psi}$ shows a nearly straight line variation with $\overline{\varphi}$. This is typical of the high-staggered inducer blading. It is also notable that a relatively high efficiency level (> 80 percent) extends over a large portion of the operating range. As flow is reduced to a flow coefficient value of about 0.09, measurements indicate that a reverse flow region forms in the tip region at the blade inlet. The reverse flow, or eddy, region is indicated by inlet flow angles which increase very sharply to values of 90° or more and by increases in inlet total head (fig. 9). The angle and head measurements shown in figure 9 were taken at radial locations 10, 30, and 50 percent of the passage height from the tip. Limit switches prevent the instruments from turning past angles of approximately 100°.

At the radial location 10 percent of passage height from the tip β_1 begins a sharp increase at a $\overline{\varphi}$ of approximately 0.09 and rises to values of $\approx 100^O$ where the limit switches cut them off. The inlet total head H_1 increases to a value approximately 10 percent higher than the nearly constant level across the remainder of the passage. With reductions in flow to values below 0.09, the same general patterns are observed in β_1 and H_1 at radial stations 30 and 50 percent of the passage height from the tip. A comparison of the measurements at the three radial positions indicates the growth of the eddy region as flow is reduced.

At operating points below approximately 0.09, where the eddy flow regions have significant effects on the inlet flow measurements, mass-averaged calculations become less meaningful as noted previously. Average performance data is presented only for essentially eddy-free operation. It is of interest to note, however, that even with the eddy flows, rig vibrations did not become excessive during operation down to $\overline{\varphi} \sim 0.05$.
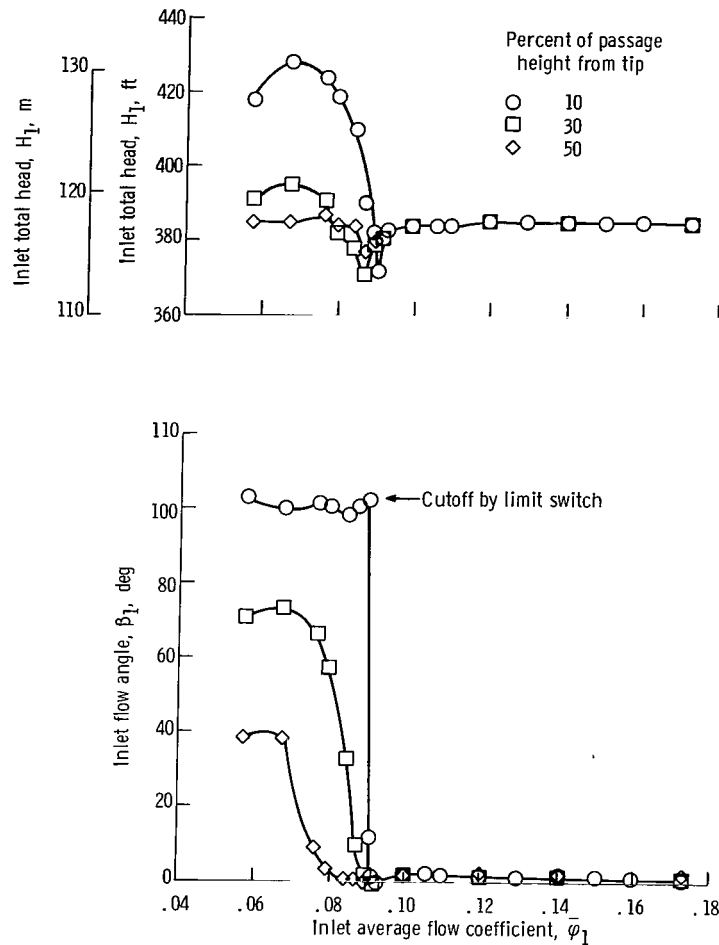
Figure 9. – Variation of inlet flow angle and total head with flow at three passage locations.

Cavitating Average Performance

Cavitation performance was determined using two different test procedures. In the first procedure the net positive suction head H_{sv}, was held constant while flow was varied. In the second, the flow was held constant while the H_{sv} was varied.

The variations of head rise with flow while H_{sv} was maintained constant are presented in figures 10 and 11. The head rise coefficient of figure 10 is that measured across the midspan blade section and is referred to herein as midpoint data. This type of data allows an approximate mapping of the effects of cavitation on performance. Mass averaged results at selected operating points at which detailed measurements were made are presented in figure 11. In both figures noncavitating performance values are included to give a base operating level.
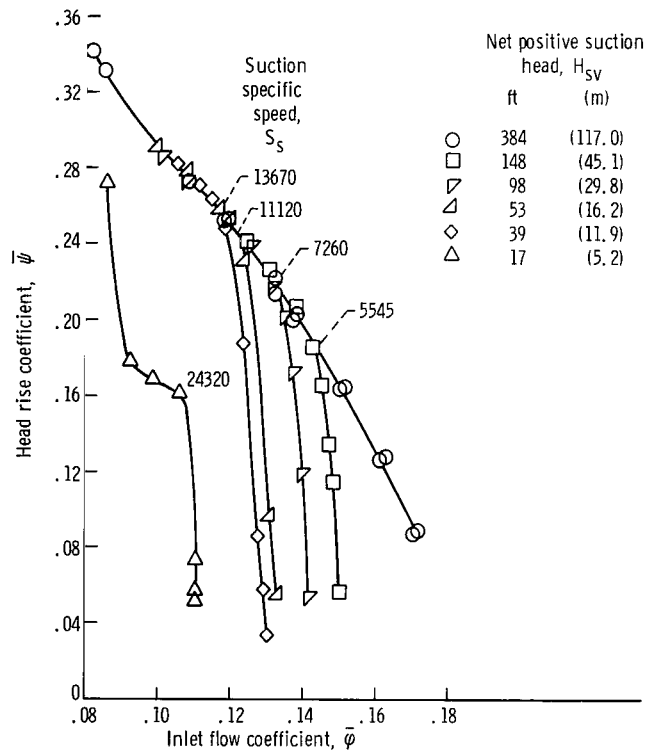
Figure 10. - Midpoint performance under cavitating and noncavitating conditions.
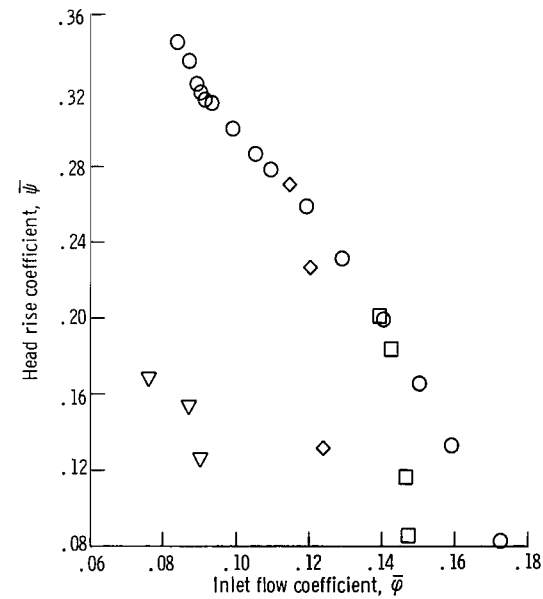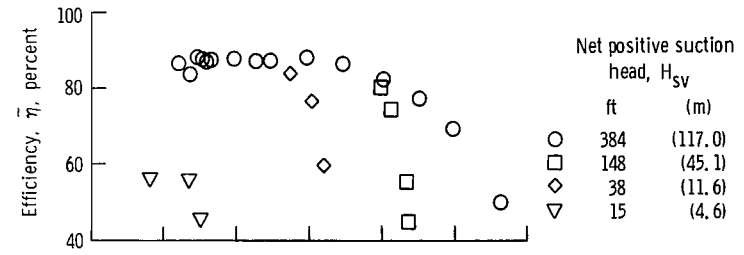

Figure 11. - Overall performance under cavitating and noncavitating conditions.

In general, the plots of figures 10 and 11 indicate that cavitation causes a dropoff in head rise and efficiency and a decrease in the maximum flow attainable. The suction specific speed S_s values on figure 10 indicate the maximum S_s at which this inducer can operate noncavitating at the particular values of flow coefficient indicated. An extrapolation of these values to the design flow coefficient of 0.107 indicates that cavitation would affect performance above a S_s of approximately 20 000. At design flow and an H_{sv} of 17 feet, which results in a S_s of approximately 24 300, the measured head rise is 57 percent of the noncavitating value, while the maximum flow for this H_{sv} is only about 4 percent higher than the design value. The plots of figure 11 indicate that at an H_{sv} of 15 feet, design flow could not be attained.

Results from tests in which flow is held constant and H_{sv} varied are shown in figures 12 and 13. The head rise shown in figure 12 is that measured across the midspan
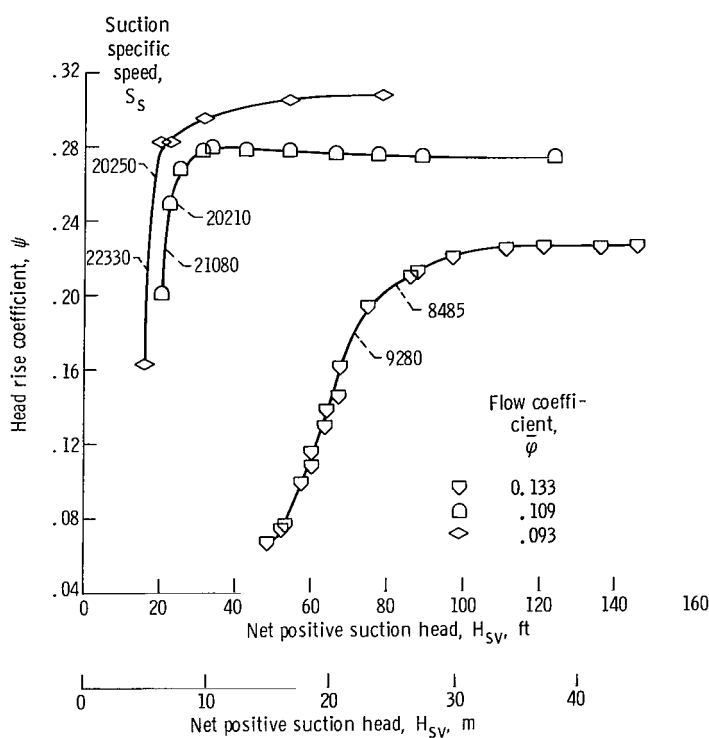

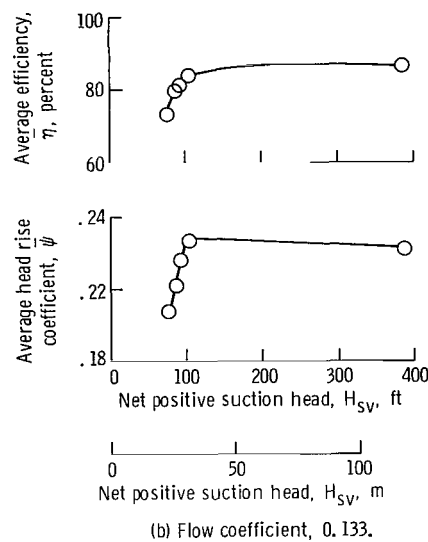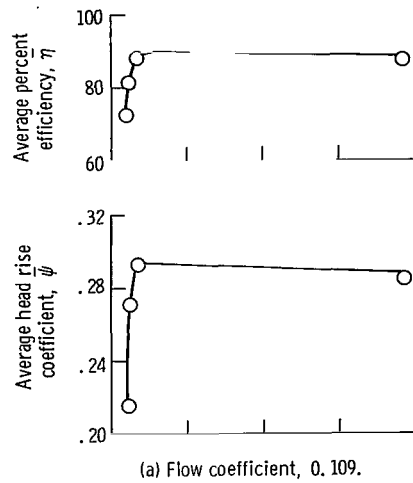Figure 12. - Effect of cavitation on inducer midpoint head rise coefficient.

(a) Flow coefficient, 0.109.

(b) Flow coefficient, 0.133.

Figure 13. - Effects of cavitation on in-
ducer overall head-rise and efficiency.

of the blade (midpoint data). The head rise and efficiency values of figure 13 result from
mass-averaged measurements across the complete blade span. The midpoint data
employs a large number of data points and provides a better definition of inducer per-
formance. The averaged data give the more realistic levels of performance.

The curves generally indicate the effect on inducer performance as the inlet pres-
sure is reduced. On figure 12 the suction specific speed values at which the inducer head
rise has decreased 10 and 20 percent below the noncavitating levels are listed. Cavitation
at near-design flow ($\bar{\varphi} = 0.109$) causes a rather sharp dropoff in the head rise as H_{sv}
is reduced. A 10-percent decrease of head rise occurred at a S_s of approximately

15
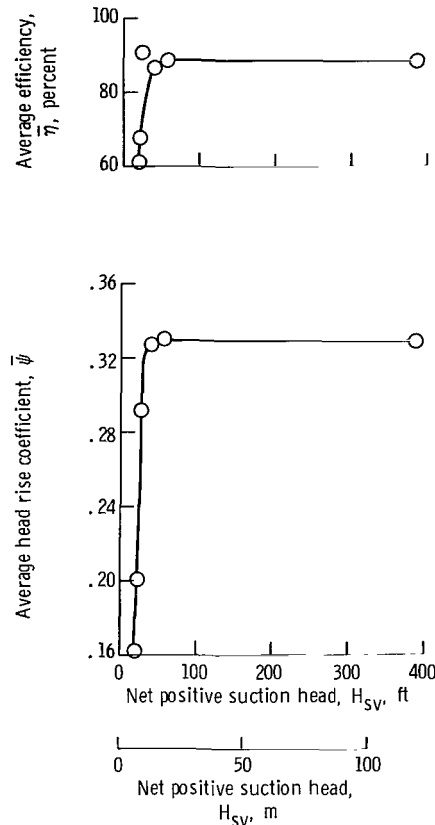
(c) Flow coefficient, 0.092.

Figure 13. – Concluded.

20 000. By comparison, the two rotating blade rows comprising the inducer of a two-stage pump (ref. 1), and flat plate inducers (refs. 5 to 7) achieved a S_s of from 25 000 to 27 000 before similar head decreases were observed.

One means by which the cavitation performance of this tandem inducer might be improved is by altering the blade thickness distribution in the leading edge region of the front and rear blades. A distorted sketch (thickness scale is 10 times the chord length scale) of the front blade section at the tip is shown in figure 14. Superimposed on the blade section are calculated cavity shapes for various suction specific speed values (at design flow coefficient). The method used to compute the cavity shapes is discussed in detail in reference 9. The cavity shapes for helical blades are computed from inputs of helix angle, flow coefficient, and suction specific speed. The blade leading edge should be faired to lie within the computed cavity to avoid the detrimental effects of blade thickness. This procedure was applied to the tip blade element of the front blade for $\overline{\varphi} = 0.109$, and the helix angle of the blade pressure surface. The cavity was assumed to start at the foremost point of the leading edge as shown. Cavity shapes for S_s of
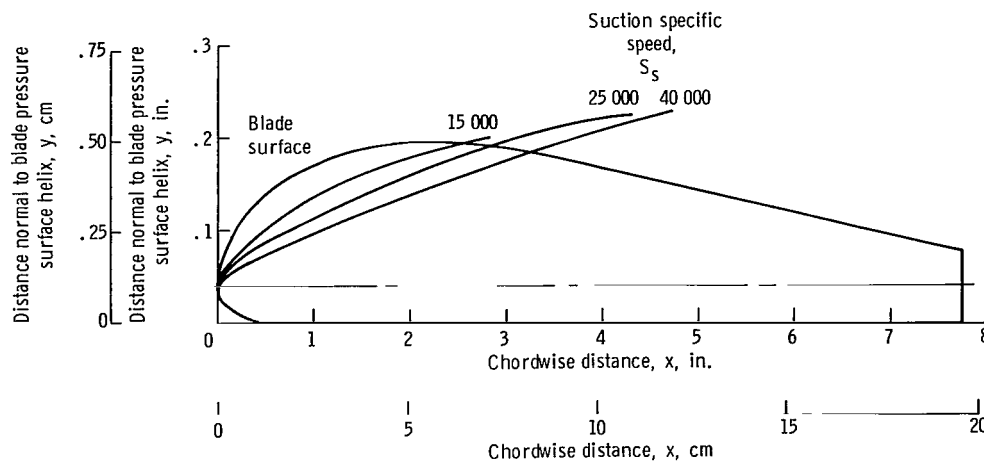
Figure 14. – Comparison of front vane tip profile (6.50-in. (16.51-cm)) diameter with theo-
retical cavity shapes based on pressure surface helix and flow coefficient of 0.109.

15 000, 25 000, and 40 000 were calculated. The sketch in figure 14 shows that portions of the blade in the leading edge region lie outside the computed cavity shapes for all S_s values considered.

The comparisons indicate the desirability of reducing blade thickness in the inlet portions of the front blade as a means of obtaining improved cavitation performance. It is further speculated that similar reductions in blade thickness may be desirable on the rear blade for best overall gains in cavitation performance. Visual observations (which follow), indicate that significant decreases in inducer head rise due to cavitation do not occur until cavitation is observed on the rear blade.

Visual Observations

Visual observations of the flow were made at both cavitating and noncavitating flow conditions. To aid in visualizing flow direction in the tip region, tufts were mounted on the outer wall plastic casing. The first row of tufts upstream of the rotor leading edge (5th row from the left in fig. 15) lies in the plane of the inlet flow measuring station.

A sequence of photographs showing flow conditions at an H_{sv} equivalent to 384 feet at design rotor speed and a range of flow rates is shown in figure 15. The flow conditions of figure 15 were presented previously (fig. 8) as the noncavitating overall performance characteristic. Visual results are related to performance results by positioning the photographs on the approximate location of each on the overall performance characteristic.

Visual observations indicate that over the flow range covered, the flow was essen-
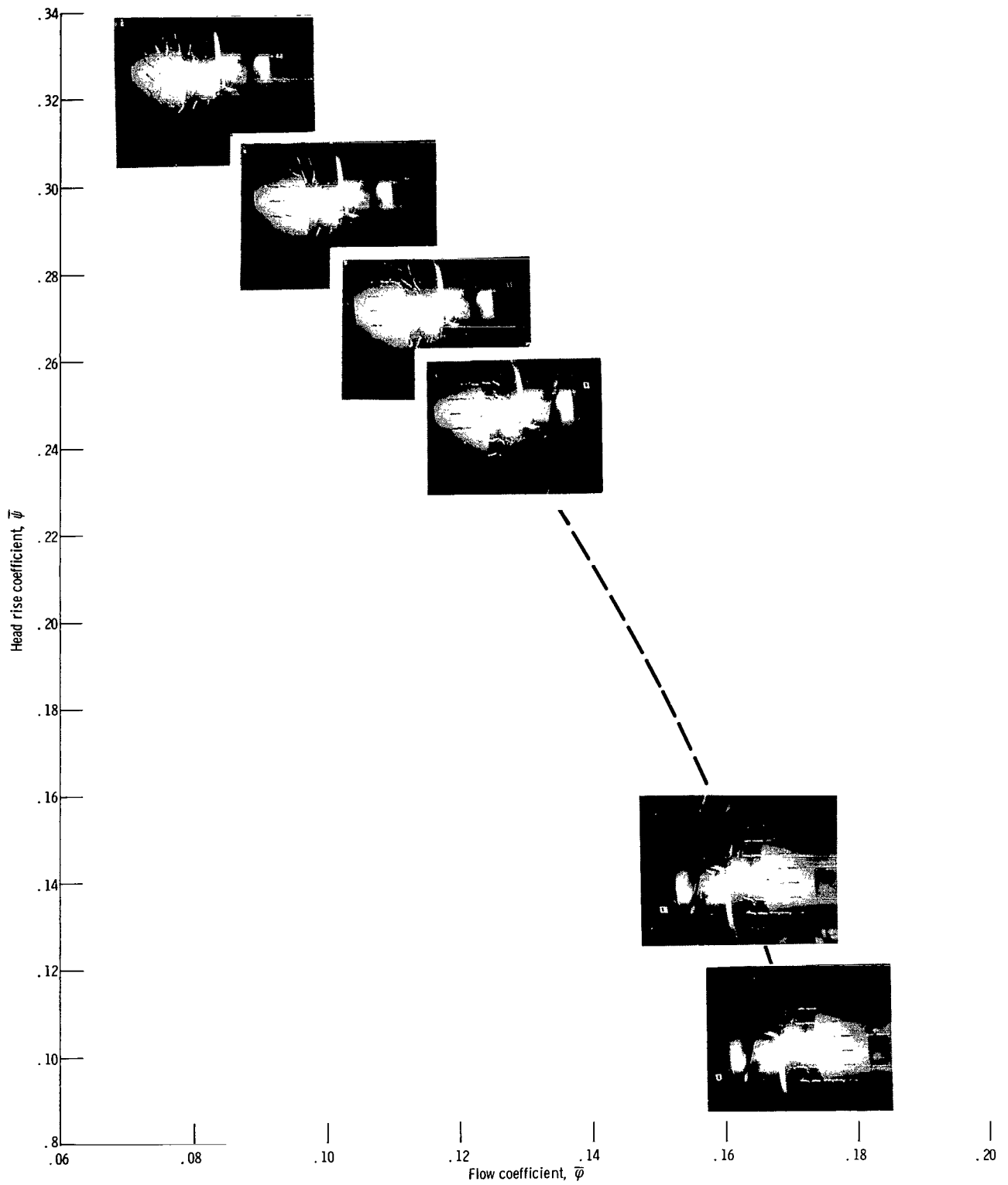
Figure 15. - Flow conditions over range of flows for noncavitating performance.   Net positive suction head, 384 feet (117 m).

tially free of both tip clearance and blade surface cavitation except at the highest flow rate. At $\overline{\varphi} = 0.171$ a small amount of blade surface cavitation in the blade leading edge region and tip clearance flow cavitation is observed on the rear blade (bottom photograph of fig. 15). Over the flow coefficient range from a maximum value ($\overline{\varphi} = 0.171$) to a value near $\overline{\varphi} = 0.12$, the outer wall tufts indicate that the fluid flows directly into the rotating blade row. At $\overline{\varphi} \sim 0.110$, the tufts in the inlet measuring plane (row 5 from the left) indicate a significant prewhirl (in the direction of rotor rotation) in the inlet flow. As flow is reduced from $\overline{\varphi} \sim 0.110$, the tufts show an increase in both the magnitude of the prewhirl and the upstream extent of the prewhirl region. At some locations the tuft directions indicate a reverse flow component to the flow in this tip region.

At the radial measuring station nearest the outer wall (0.195 in. (0.495 cm) from the outer wall), the flow angle measurements indicated an inlet prewhirl velocity component at $\overline{\varphi} \sim 0.09$ (see fig. 9). This agrees with the visual data.

Sequences of photographs showing the start and growth of cavitation as inlet pressure is reduced are presented in figure 16. The three flow rates presented include a flow rate near design value ($\overline{\varphi} = 0.106$ in fig. 16(a)), a high flow rate ($\overline{\varphi} = 0.130$ in fig. 16(b)), and a low flow rate ($\overline{\varphi} = 0.090$ in fig. 16(c)). The visual data is related to the performance data by positioning the photographs on the $\overline{\psi}$ against H_{SV} characteristics.

At a flow near design (fig. 16(a)), as H_{SV} is reduced, both blade surface and tip clearance cavitations are observed first on the leading edge region of the rear blade near an H_{SV} of about 75 feet (22.8 m). Evidently in spite of some anticipated static pressure increase across the front blade, the acceleration of flow through the slot and around the leading edge portion of the rear blade is sufficient to drop the local pressure below vapor pressure and initiate cavitation in this region first. As H_{SV} is further reduced, cavitation occurs on both the front and rear blades and increases in both the intensity and the chordwise extent. However, a significant decrease in head rise is not observed until the cavitation extends over a major portion of both blades.

At a flow higher than design ($\overline{\varphi} = 0.130$ on fig. 16(b)), as H_{SV} was reduced, cavitation occurred first on the rear blade at an H_{SV} of about 120 feet (36.6 m). As H_{SV} is further reduced, the cavitation on the rear blade intensifies and extends over greater chordwise distances. Only minor amounts of cavitation are observed on the front blade and this occurs in the trailing edge region. At this flow the dropoff in head rise due to cavitation is apparently caused by effects on the performance of the second blade.

At a low flow rate ($\overline{\varphi} = 0.090$ in fig. 16(c)), as H_{SV} was reduced, cavitation was observed on the front blade at an H_{SV} of about 90 feet (27.4 m). As H_{SV} is further reduced the cavitation intensifies and extends over increasing chordwise portions of the front blade with the rear blade cavitation-free. Eventually the cavitation extends over the total chordwise distance of both front and rear blades. A significant decrease in
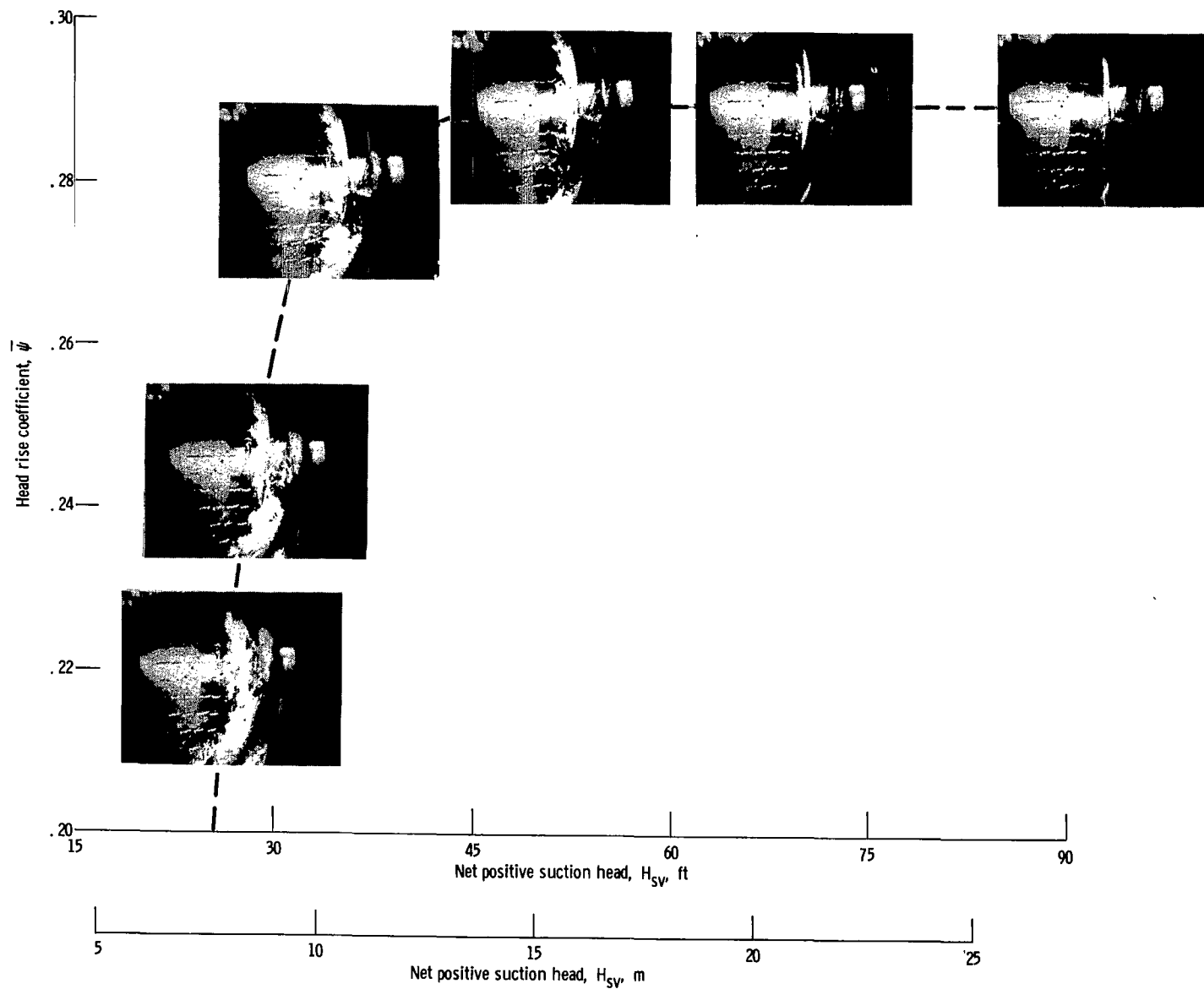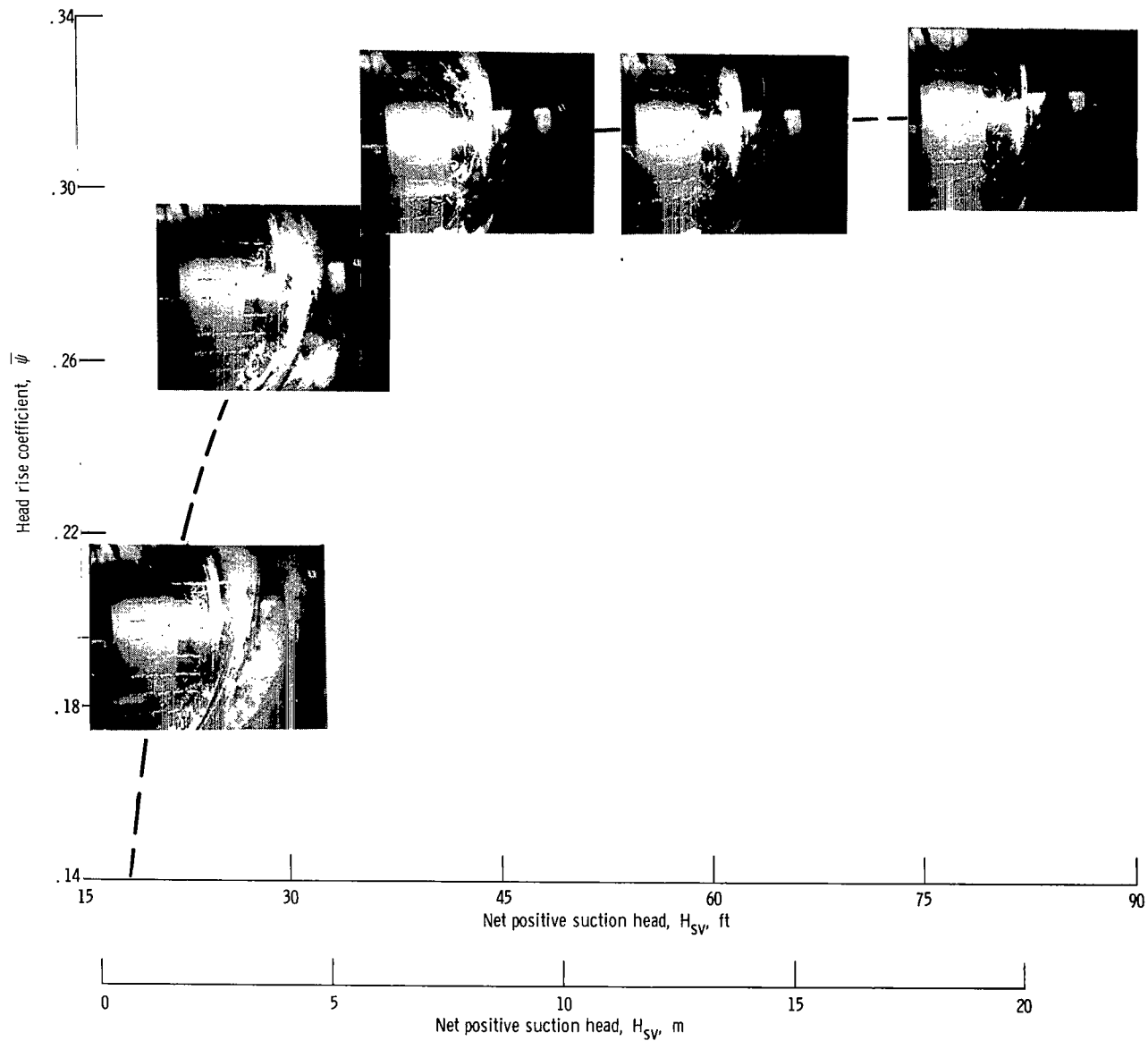
(a) Flow coefficient, 0. 106.

Figure 16. - Changes in cavitation for constant flow rate and varying net positive suction head.

Head rise coefficient, ψ

Net positive suction head, H_{sv}, ft

Net positive suction head, H_{sv}, m
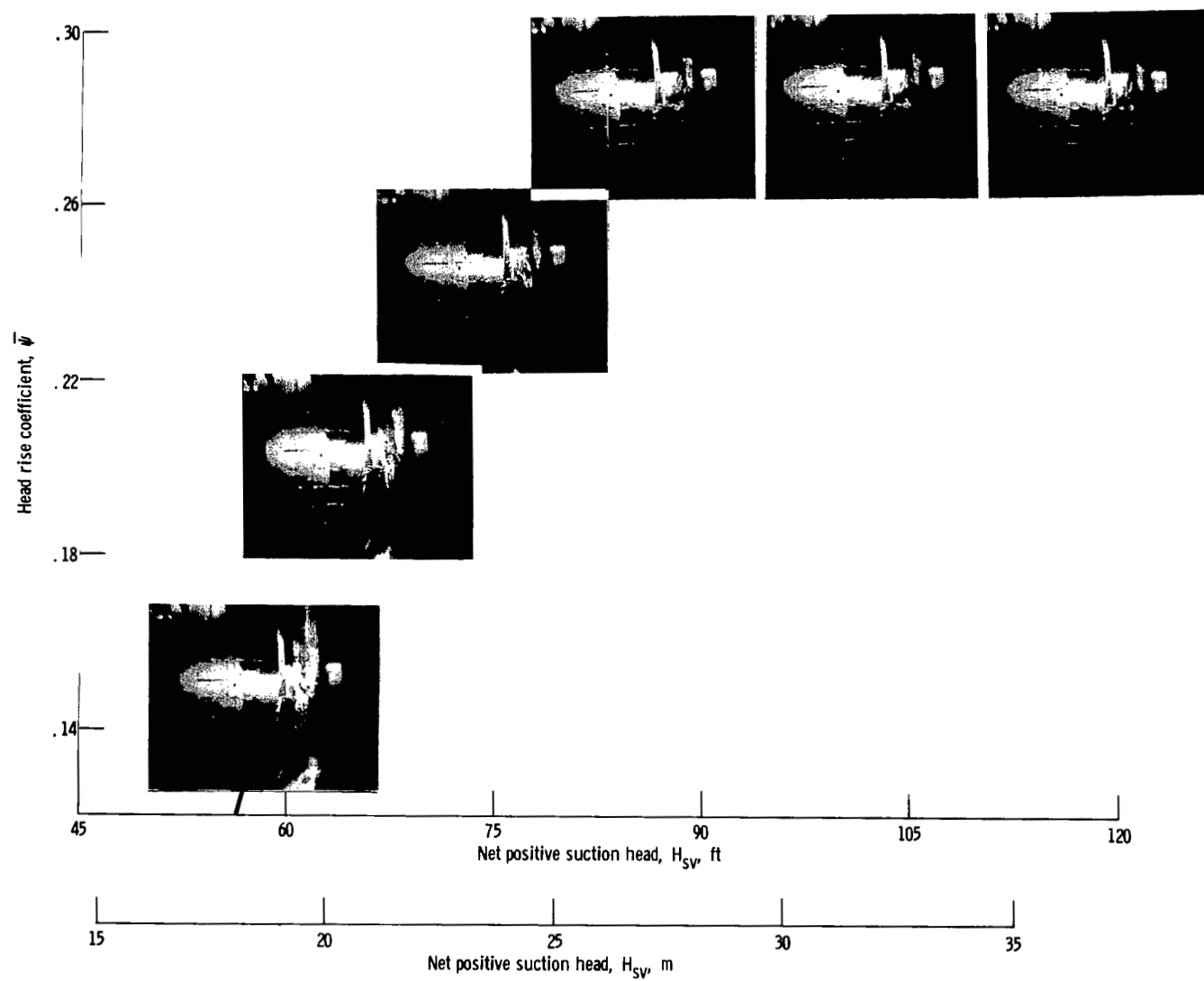
(b) Average flow coefficient, 0.130.

Figure 16. – Continued.

(c) Average flow coefficient, 0.090.

Figure 16. - Concluded.

head rise occurred only after cavitation began to affect the rear blade performance. At the highest H_{sv} value shown ($H_{sv} \sim 90$ ft), the tufts on the outer wall nearest the front blade leading edge indicate a prewhirl and even reverse flows. As H_{sv} is reduced and the increased cavitation in the blade leading edge region tends to reduce the blade loading in that region, the prewhirl and reverse flows are gradually reduced and eventually eliminated.

During all the observations of cavitation made in the course of this investigation, it is notable that no form of an unsteady cavitation was observed. In this type of cavitation the cavity length can be observed to oscillate at some frequency. This phenomenon is generally observed at H_{sv} values close to those at which the head rise dropoff occurs. This form of cavitation has been observed during investigations of flat plate inducers (ref. 5) and plano-convex hydrofoils in cascade (ref. 10).

Some Effects of Slot Configuration

In the design of this inducer configuration, the trailing edge of the front blade and the leading edge of the rear blade lie in the same meridional plane (see fig. 2). This configuration is referred to as tandem I. Small changes to the slot geometry were made by moving the rear blade circumferentially approximately 0.1 inch from this design plane both opposite to the direction of rotation (tandem II), and in the direction of rotation (tandem III). The effect of these changes on slot configuration can be visualized from the sketch shown in figure 17 and the photographs of figure 18.
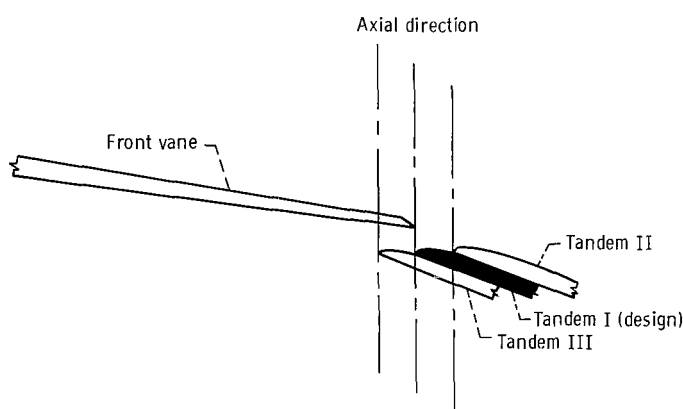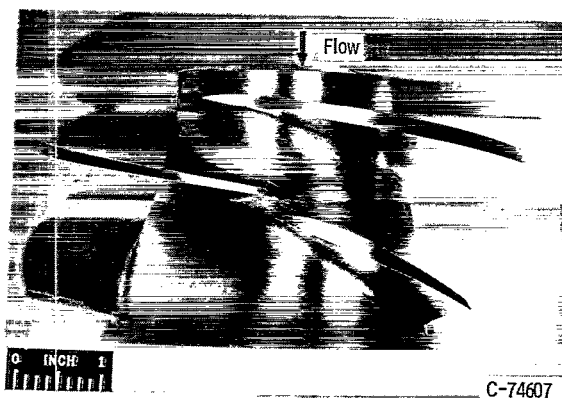

Figure 17. – Changes in slot geometry as rear vane of tandem inducer is moved circumferentially (not to scale).

(a) Tandem I. Design configuration.

(b) Tandem II. Rear vane moved opposite to direction of rotation.

(c) Tandem III. Rear vane moved in direction of rotation.

Figure 18. – Tandem inducer with rear vane in three circumferential locations.
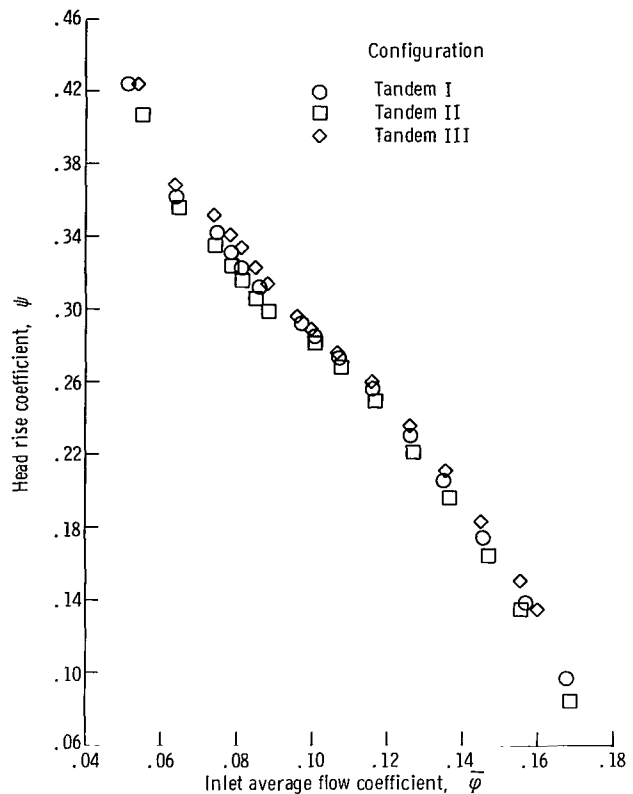
Figure 19. – Comparison of noncavitating midspan head rise characteristics from three tandem inducer configurations.

The noncavitating results for the three configurations are compared on figure 19. For this phase of the investigation, only midspan head rise was measured. The variations in head rise are generally small but consistent over the complete flow range. When the rear blade was moved in the direction opposite to the direction of rotation (tandem II), the head rise is slightly decreased from that produced by the design configuration (tandem I). When the rear blade is moved in the direction of rotation (tandem III), the head rise is slightly increased from that produced by the design configuration (tandem I). Also the differences of head rise with changes in rear blade position are larger in both the high flow and low flow regions.

From the sketch of figure 17 and the photograph of figure 18 several reasons for the variation in head rise with rear blade position are suggested. As the rear blade is moved in the direction of rotation (tandem III), the rear blade displaced a greater distance from the front blade wake, and the slot configuration gives improved guidance to the slot flow over the suction surface of the rear blade. It is thus anticipated that this change would tend to improve performance. Movement of the rear blade opposite to the direction of rotation (tandem II) produces contrasting effects.
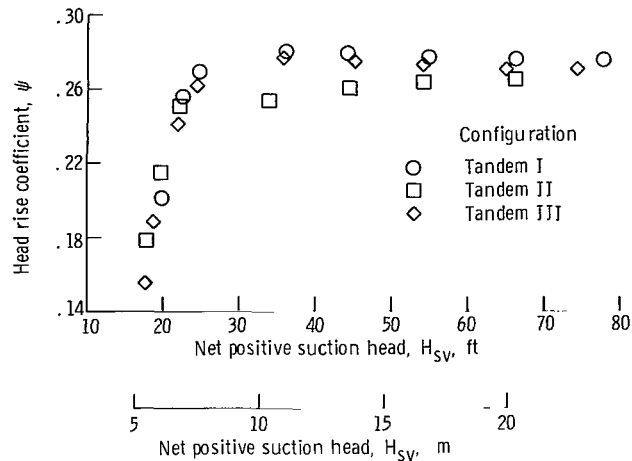
Figure 20. – Comparison of effects of cavitation on midspan head rise coefficient for three tandem inducer configurations. Flow coefficient, 0.109.

The effects of the slot geometry changes on cavitating performance near design flow are shown in figure 20 where midpoint ψ is plotted as a function of H_{sv} for the three configurations. The plots indicate cavitation breakdown occurs at approximately the same H_{sv} ($\sim$ 22 ft) (6.7 m) for all configurations. Tandem I and III configurations show no measurable effects of cavitation as H_{sv} is reduced until the degree of cavitation reaches that required for a complete breakdown in head rise, whereas tandem II configuration shows a gradual decrease in head rise as H_{sv} is lowered and the amount of cavitation increases.

SUMMARY OF RESULTS

A 6.5 inch (16.5 cm) diameter inducer with tandem blades was tested in cold water to determine the noncavitating and cavitating performance. The inducer was designed to produce a head rise coefficient of 0.303 at an inlet ideal flow coefficient of 0.109.

From the test results the following specific results were indicated:

1. Under noncavitating flow conditions the tandem blade inducer produced a mass-averaged head rise coefficient of 0.278 at a hydraulic efficiency of approximately 88 percent at design flow. Both these values represent relatively high levels of inducer performance.

A relatively high hydraulic efficiency ($>$ 80 percent) was maintained over a large portion of the flow range. At a flow of approximately 84 percent of design, measurements indicated a reverse flow, or eddy, region in the flow entering the blade tip. As flow was reduced from this value, the radial extent of the eddy region increased.

26

2. Under cavitating flow conditions at design flow, cavitation caused a 10-percent decrease in head rise from the noncavitating level at a suction specific speed of approximately 20 000. This moderate suction performance is attributed to excessive thickness in the inlet portion of both the front and rear blades. Visualization of flow indicated that cavitation did not cause a dropoff in inducer head rise from the noncavitating level until the cavitation was present in the passages of the rear blades.

3. Some variation in blade overlap (or slot geometry) was investigated and data were taken at the midspan location. As the overlap of the two blades was increased, the noncavitating head rise increased. Breakdown of inducer head rise due to cavitation occurred at approximately the same suction specific speed for the three configurations tested.

4. From outer wall boundary layer measurements, flow blockage values of 2.20 percent at the blade inlet and 2.29 percent at the blade outlet were computed at design flow. Boundary layer velocity profiles and selected parameters are presented.

Lewis Research Center,
    National Aeronautics and Space Administration,
        Cleveland, Ohio, January 8, 1969,
            128-31-32-12-22.

APPENDIX A

SYMBOLS

A	area, in.^{2} (cm^2)
A_b	blockage area
d	diameter, in. (cm)
g	acceleration due to gravity, 32.17 ft/sec^2 (9.805 m/sec^2)
H	total head, ft (m)
ΔH	blade-element head rise, ft (m)
H_{sv}	net positive suction head, ft (m)
h_v	vapor pressure head, ft (m)
N	rotative speed, rpm
Q	flow rate, gal/min (m^3/min)
r	radius, ft (m)
S_s	suction specific speed
t_{max}	maximum thickness, in (cm)
U	rotor tangential velocity, ft/sec (m/sec)
V	absolute velocity, ft/sec (m/sec)
x, y	directional coordinate, in. (cm) (defined in fig. 2)
β	flow angle with respect to axial direction, deg
δ	limit of integration - in. (cm)
$\delta*$	boundary layer displacement thickness, in. (cm)
η	rotor efficiency
φ	flow coefficient, V_z/U_t
ψ	head rise coefficient, $g \Delta H/U_t^2$
θ	boundary layer momentum thickness, in. (cm)

Subscripts:

f.s.	free stream
h	hub
id	ideal

LE   leading edge

T   total

t   tip

v   measured with Venturi meter

z   axial component

θ tangential direction

1   inlet

2   outlet

Superscript:

—   average quantity

APPENDIX B

EQUATIONS

$$\overline{\Delta H} = \overline{H}_2 - \overline{H}_1 = \frac{\sum\limits_{j=1}^{j=4}\left(r_j V_{z,2,j}H_{2,j} + r_{j+1}V_{z,2,j+1}H_{2,j+1}\right)\left(r_j - r_{j+1}\right)}{\sum\limits_{j=1}^{j=4}\left(r_j V_{z,2,j} + r_{j+1}V_{z,2,j+1}\right)\left(r_j - r_{j+1}\right)}$$

$$-\frac{\sum\limits_{j=1}^{j=4}\left(r_j V_{z,1,j}H_{1,j} + r_{j+1}V_{z,1,j+1}H_{1,j+1}\right)\left(r_j - r_{j+1}\right)}{\sum\limits_{j=1}^{j=4}\left(r_j V_{z,2,j} + r_{j+1}V_{z,2,j+1}\right)\left(r_j - r_{j+1}\right)} \qquad (B1)$$

$$\overline{\Delta H}_{id} = \frac{1}{g}\left(\overline{U_2 V}_{\theta,2} - \overline{U_1 V}_{\theta,1}\right)$$

$$= \frac{1}{g}\left(\frac{\sum\limits_{j=1}^{j=4}U_{2,j}V_{\theta,2,j}A_{2,j}V_{z,2,j}}{\sum\limits_{j=1}^{j=4}A_{2,j}V_{z,2,j}} - \frac{\sum\limits_{j=1}^{j=4}U_{1,j}V_{\theta,1,j}A_{1,j}V_{z,1,j}}{\sum\limits_{j=1}^{j=4}A_{1,j}V_{z,1,j}}\right) \qquad (B2)$$

$$\overline{\eta} = \frac{\overline{\Delta H}}{\overline{\Delta H}_{id}} \qquad (B3)$$

$$\overline{\psi} = \frac{g\,\overline{\Delta H}}{U_{t_2}^2} \qquad (B4)$$

$$\overline{\varphi}_1 = \frac{Q_v}{448.8\,\pi\left(r_{t_1}^2 - r_{h_1}^2\right)U_{t_1}} \qquad (B5)$$

$$H_{sv} = H_1 - h_v \tag{B6}$$

$$S_s = \frac{NQ^{1/2}}{H_{sv}^{3/4}} \tag{B7}$$

$$\delta^* = \int_0^\delta \left(1 - \frac{V_z}{V_{z,f.s.}} \right) dy \tag{B8}$$

$$\theta = \int_0^\delta \frac{V_z}{V_{z,f.s.}} \left(1 - \frac{V_z}{V_{z,f.s.}} \right) dy \tag{B9}$$

$$\text{Form factor} = \frac{\delta^*}{\theta} \tag{B10}$$

APPENDIX C

OUTER WALL BOUNDARY LAYER MEASUREMENTS

Surveys of flow conditions across the outer wall boundary layer were made at the blade inlet and outlet measuring stations for a range of flows. For this investigation, these measurements were used primarily to study flow blockage values. However, for interest, the measured velocity profiles and selected boundary layer parameters are presented.

The velocity profiles obtained at the blade inlet measuring station are shown in figure 21. The velocities are computed from boundary layer surveys of total pressures and angles and wall static pressure measurements. The boundary layer parameters, displacement thickness δ^*, momentum thickness θ, and form factor were computed from the velocity profiles shown and these values are listed in the figure. At the inlet measuring station, angle measurements indicated that the flow direction was essentially axial
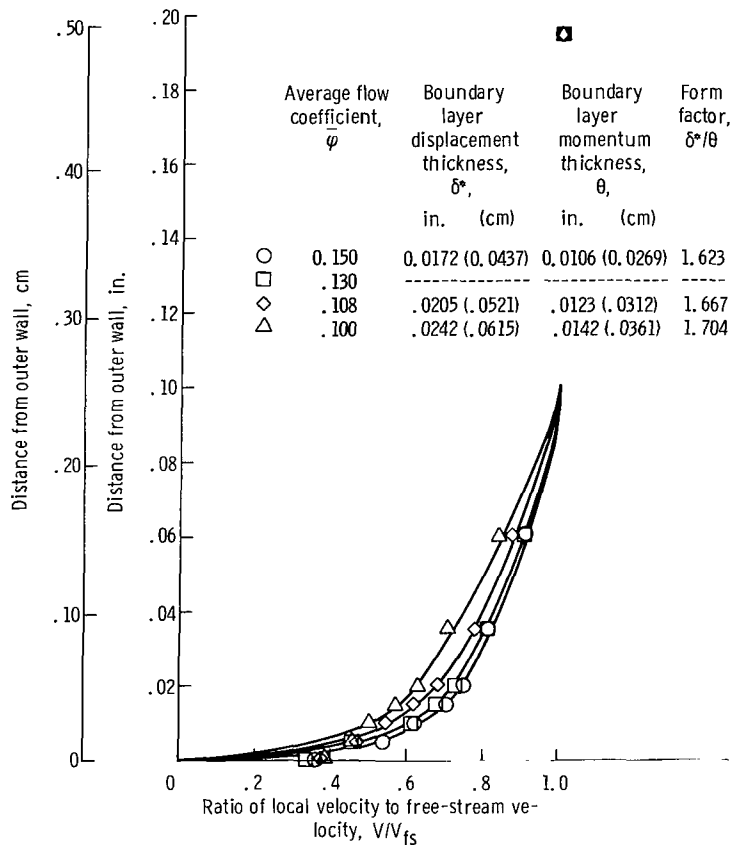

Figure 21. - Distribution of velocity across outer-wall boundary layer at inducer inlet.

and thus, the boundary layer was considered two-dimensional. The velocities are presented as the ratio of local velocity to free-stream velocity. Free-stream velocity (fig. 21) is the value measured at the radial location 0.195 inch (0.495 cm) from the outer wall. As shown in figure 21 surveys of inlet velocity indicated that the free-stream value was maintained to a radial location approximately 0.100 inch (0.254 cm) from the outer wall. Thus, the boundary layer thickness was set at 0.100 inch (0.254 cm) in all flow parameter calculations. Using the computed values of displacement thickness δ^*, and assuming that the same value of δ^* occurred on the hub shroud, area blockage factors were computed. These are presented in the following table as the ratio of the blocked

Flow coefficient, $\overline{\varphi}$	Ratio of blocked area to total annulus area, percent		
	Outer wall, $(A_b/A)_{OW}$	Inner wall, $(A_b/A)_{IW}$	Total, $(A_b/A)_T$
0.150	1.13	0.51	1.64
.108	1.58	.62	2.20
.100	1.80	.71	2.51

area (A_b) to the total annulus area (A) in percent. These values were computed at both the outer wall (OW) and the inner wall (IW). The total blocked area is the sum of the outer and inner wall values. At the ideal design flow coefficient of 0.109, a flow blockage of about 2.20 percent is indicated. Consequently, the design inlet flow diagrams should be achieved at a measured average flow coefficient of

$$\overline{\varphi} = (0.978)\ \overline{\varphi}_{id} = 0.107$$

The flow coefficient of 0.107 was used as the design value in comparisons of measured and design performance.

As flow coefficient is reduced from $\overline{\varphi} = 0.15$ to $\overline{\varphi} = 0.10$ a consistent increase in both δ^* and θ are noted (fig. 21). These increases in the deficiencies of mass flow area and momentum in the flow probably result from a sensing of the increasing static head rise across the rotor as flow is reduced. No boundary layer measurements were taken at flow coefficients less than 0.10 because of indications of reverse flow regions as previously discussed.

At the blade outlet measuring station, the boundary layer flow has both axial and tangential velocity components. This skewed boundary layer flow is further complicated by the 0.014 inch (0.035 cm) tip clearance between the housing and the rotating blade row. For these reasons calculation of boundary layer parameters at this station was limited to
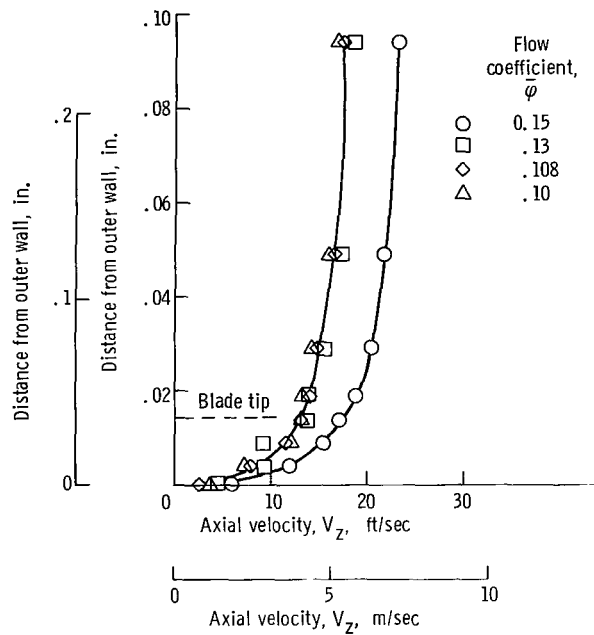
Figure 22. - Distribution of axial velocity across outer-wall boundary layer at inducer outlet.
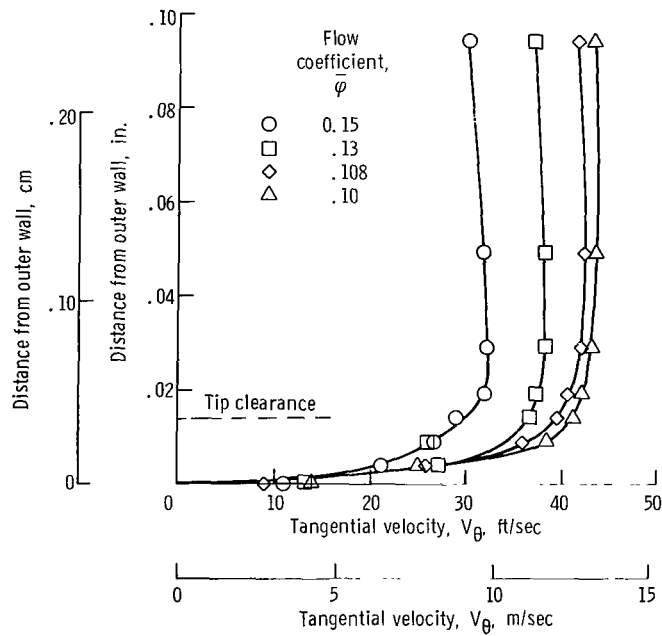

Figure 23. - Distribution of tangential velocity across outer-wall boundary layer at inducer outlet.

a displacement thickness. The axial and tangential components of the boundary layer velocities are presented in figures 22 and 23, respectively. A comparison of the boundary layer surveys with the passage surveys indicated that measurements at a location approximately 0.050 inch (0.127 cm) from the outer wall could be used as free-stream values.

At the inducer outlet measuring station, the boundary layer measurements show an increase in tangential velocity (fig. 23) as the weight flow is decreased. This is consistent with the general increase in incidence angle and lower average axial velocity for all blade sections. The tangential velocity V_θ also serves as a measure of blade element circulation. The V_θ distributions indicate that the blade element circulation is maintained to the blade tip and drops off in a consistent manner across the blade tip clearance region.

The axial velocity distributions (fig. 22) show a significant decrease from operation at $\overline{\varphi} = 0.15$ to $\overline{\varphi} = 0.13$ as would be predicted. At flows below $\overline{\varphi} = 0.13$ radial equilibrium requirements, as influenced by radial gradients of loss and energy addition, were such that the axial velocity in the tip region showed little or no change. When the ratio of local axial velocity to the free-stream value was plotted, a single faired curve was used (fig. 24) to compute a value of $\delta*$ (0.0097). The calculation followed the simple two-dimensional boundary layer approach (similar to that applied to the inlet measurements) and was based on axial velocity components. Two observations are made from this data:

(1) The $\delta*$ at the blade outlet is smaller than that computed at the blade inlet measuring station.
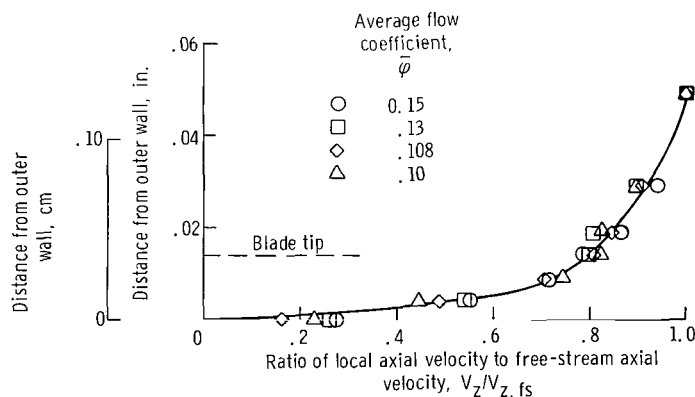

Figure 24. - Distribution of axial velocity ratio across outer-wall boundary layer at inducer outlet. Boundary layer displacement thickness, 0.0097 inch (0.0246 cm).

(2) The $\delta*$ at the blade outlet did not vary consistently with flow even though the static pressure change across the inducer rotor approximately doubled as $\overline{\varphi}$ was decreased from 0.15 to 0.10.

Applying the $\delta*$ value of 0.0097 (inches) to both the inner and outer walls, the following constant area blockage factors (in percent) were computed (using axial velocity V_Z) for $\overline{\varphi}$ from 0.10 to 0.15:

Outer wall, $(A_b/A)_{OW}$	Inner wall, $(A_b/A)_{IW}$	Total, $(A_b/A)_T$
1.38	0.91	2.29

When comparing the area blockage factors computed for the inlet and outlet measuring stations, it should be recognized that (1) geometric annulus flow areas at the inlet and outlet differ by a factor of two and (2) both the outer wall and inner wall radii at which the displacement thicknesses are applied, differ at the two axial locations.

REFERENCES

1. Sandercock, Donald M.; and Crouse, James E.: Design and Overall Performance of a Two-Stage Axial-Flow Pump with a Tandem-Row Inlet Stage. NASA TN D-2879, 1965.

2. Sheets, H. E.: The Slotted-Blade Axial-Flow Blower. Trans. ASME, vol. 78, no. 8, Nov. 1956, pp. 1683-1690.

3. Sheets, Herman E.; and Brancart, Claude P.: A Multi-stage Slotted Blade Axial Flow Pump. J. Eng. Power, vol. 88, no. 2, Apr. 1966, pp. 105-110.

4. Railly, J. W.: and El-Sarha, M. E.: An Investigation of the Flow Through Tandem Cascades. Proc. Inst. Mech. Engrs., vol. 180, pt. 3J, 1965-1966, pp. 66-73.

5. Soltis, Richard F.; Anderson, Douglas A.; and Sandercock, Donald M.: Investigation of the Performance of a 78° Flat-Plate Helical Inducer. NASA TN D-1170, 1962.

6. Sandercock, Donald M.; Soltis, Richard F.; and Anderson, Douglas A.: Cavitation and Noncavitation Performance of an 80.6^O Flat-Plate Helical Inducer at Three Rotational Speeds. NASA TN D-1439, 1962.

7. Anderson, Douglas A.; Soltis, Richard F.; and Sandercock, Donald M.: Performance of 84° Flat-Plate Helical Inducer and Comparison with Performance of Similar 78° and 80.6^O Inducers. NASA TN D-2553, 1964.

8. Crouse, James E.; Montgomery, John C.; and Soltis, Richard F.: Investigation of the Performance of an Axial-Flow-Pump Stage Designed by the Blade-Element Theory-Design and Overall Performance. NASA TN D-591, 1961.

9. Stripling, L. B.; and Acosta, A. J.: Cavitation in Turbopumps-Part I. J. Basic Eng., vol. 84, no. 3, Sept. 1962, pp. 326-338.

10. Wade, R. B.; and Acosta, A. J.: Experimental Observations on the Flow Past a Plano-Convex Hydrofoil. J. Basic Eng., vol. 88, no. 1, Mar. 1966, pp. 273-283.

"The aeronautical and space activities of the United States shall be conducted so as to contribute . . . to the expansion of human knowledge of phenomena in the atmosphere and space. The Administration shall provide for the widest practicable and appropriate dissemination of information concerning its activities and the results thereof."

— NATIONAL AERONAUTICS AND SPACE ACT OF 1958

NASA SCIENTIFIC AND TECHNICAL PUBLICATIONS

TECHNICAL REPORTS: Scientific and technical information considered important, complete, and a lasting contribution to existing knowledge.

TECHNICAL NOTES: Information less broad in scope but nevertheless of importance as a contribution to existing knowledge.

TECHNICAL MEMORANDUMS: Information receiving limited distribution because of preliminary data, security classification, or other reasons.

CONTRACTOR REPORTS: Scientific and technical information generated under a NASA contract or grant and considered an important contribution to existing knowledge.

TECHNICAL TRANSLATIONS: Information published in a foreign language considered to merit NASA distribution in English.

SPECIAL PUBLICATIONS: Information derived from or of value to NASA activities. Publications include conference proceedings, monographs, data compilations, handbooks, sourcebooks, and special bibliographies.

TECHNOLOGY UTILIZATION PUBLICATIONS: Information on technology used by NASA that may be of particular interest in commercial and other non-aerospace applications. Publications include Tech Briefs, Technology Utilization Reports and Notes, and Technology Surveys.

Details on the availability of these publications may be obtained from:

SCIENTIFIC AND TECHNICAL INFORMATION DIVISION

NATIONAL AERONAUTICS AND SPACE ADMINISTRATION
Washington, D.C. 20546